





## Predicting segregation of nonspherical particles

Ryan P. Jones <sup>1</sup>, Julio M. Ottino <sup>1,2,3</sup>, Paul B. Umbanhowar <sup>1</sup> and Richard M. Lueptow <sup>1,2,3,\*</sup>

<sup>1</sup>*Department of Mechanical Engineering, Northwestern University, Evanston, IL 60208 USA*

<sup>2</sup>*Department of Chemical and Biological Engineering, Northwestern University, Evanston, IL 60208 USA*

<sup>3</sup>*The Northwestern Institute on Complex Systems (NICO), Northwestern University, Evanston, IL 60208 USA*



(Received 6 January 2021; accepted 23 April 2021; published 18 May 2021)

Segregation, or demixing, of flowing mixtures of size-disperse noncohesive spherical particles is well understood. However, most particle systems in industry and geophysics involve nonspherical particles. Here, the segregation of bidisperse mixtures of millimeter-sized particles having various shapes is characterized using discrete element method simulations of gravity-driven free-surface granular heap flow. As a proxy for nonspherical particles, we study mixtures of cylindrical particles that vary widely in both their length and diameter ratios, including both disks and rods, as well as mixtures of cylindrical and spherical particles. The propensity to segregate is measured with a segregation length scale that characterizes the segregation velocity of the two species for these types of mixtures, identical to the approach for mixtures of spherical particles. Surprisingly, segregation can be predicted based solely on the volume ratio of the two species, regardless of particle shape. The segregation length scale increases linearly with the log of the volume ratio for volume ratios varying from 0.1 to 10 in the same way as it does for bidisperse mixtures of spherical particles. Thus, segregation properties based on spherical particles can be directly applied to nonspherical particles.

DOI: [10.1103/PhysRevFluids.6.054301](https://doi.org/10.1103/PhysRevFluids.6.054301)

### I. INTRODUCTION

Flowing mixtures of granular material, which are common in both geophysical processes and industrial settings, tend to segregate, or demix, based on differences in material properties, including size, density, surface roughness, and shape [1,2]. Nature often spontaneously sorts granular matter—wind-generated sand dunes are typically well sorted, having particles of remarkably uniform size [3]. In industrial processes, mixtures of species with different physical properties are often desirable and segregation is typically unwanted. However, achieving homogeneous particle mixtures across the wide variety of common particles varying in size, density, and shape is quite difficult. In particular, predicting particle segregation across the infinite space of particle shape remains a largely unmet challenge. Improved understanding of the drivers of segregation is necessary to effectively reduce segregation through the design of equipment, particles, or particle mixtures [4,5]; however, nearly all previous research on granular segregation has focused on spherical particles. Here we study the segregation of bidisperse mixtures of cylindrical particles (disks and rods) as well as mixtures of cylindrical particles and spherical particles with the broad goal of better understanding and accurately predicting the segregation properties of mixtures of nonspherical particles.

Segregation of mixtures of one or more nonspherical particle species has been considered in only a few previous studies. Matuttis *et al.* [6] experimentally evaluated two-dimensional (2D) segregation of equal area circles and ellipses in a vertically vibrated box and found that the ellipses

---

\*r-lueptow@northwestern.edu

rise relative to the circles. Using discrete element simulations (DEM), He *et al.* [7] studied the effect of the aspect ratio of ellipsoidal particles mixed with equal volume spheres on segregation in a rotating tumbler. They found that depending on the ellipsoid aspect ratio, the ellipsoidal particles could concentrate either in the tumbler center or at its periphery. However, they also found that a mixture of equal volume oblate and prolate ellipsoids remains mixed. The segregation of cuboids and spheres of equal edge length and diameter, respectively, in a rotating tumbler was considered by Pereira and Cleary [8]. They found that the cuboids segregate toward the tumbler center, which they attributed to differences in the surface flow velocities and energy dissipation rates of the two species. A related study using DEM simulations of shape-bidisperse mixtures of spheres and equal-volume cubes, cuboids, or ellipsoids by Lu and Müller [9] indicated that shape alone can generate radial segregation in a rotating tumbler. Alizadeh *et al.* [10] demonstrated that segregation of irregular particles (spray-dried detergent) in experiments could be accurately reproduced in DEM simulations using glued-sphere particle representations.

Perhaps the closest study to the present work, though involving a much more limited range of particles shapes, is a previous study by our group [11], which considers segregation of length-bidisperse mixtures of equal diameter, rodlike particles in a quasi-2D bounded heap flow with frictional sidewalls. The study revealed that longer rods tend to segregate upward in the flowing layer while shorter rods tend to sink and that a continuum model of granular segregation devised for spherical particles accurately predicts rodlike particle segregation. The model is based on the advection-diffusion equation with an added term for segregation [1,2]:

$$\frac{\partial c_i}{\partial t} + \nabla \cdot (\mathbf{u}c_i) + \frac{\partial}{\partial z}(w_{p,i}c_i) = \nabla \cdot (D\nabla c_i), \quad (1)$$

where  $c_i$  is the concentration of species  $i$ ,  $\mathbf{u}$  is the velocity field of the bulk flow,  $w_{p,i}$  is the segregation velocity (the  $p$  subscript is a remnant of its original application to *percolation* of size-disperse particles), and  $D$  is the collisional diffusion coefficient. The advective and diffusive terms depend on flow kinematics for which functional representations can be determined from DEM results, theory (for simple geometries), or experiments. However, the segregation term, which is the key ingredient necessary to successfully predict segregation in granular flows, is of interest here. For bidisperse granular flows of spherical particles, the simplest form for  $w_{p,i}$  for both size-varying particles of equal density [2,12–14] and density-varying particles of equal size [15] is a simplified version based on the kinetic sieving model of Savage and Lun [16] and can be expressed as

$$w_{p,i} = S_i \dot{\gamma} (1 - c_i), \quad (2)$$

where  $\dot{\gamma} = \partial u_x / \partial z$  is the local shear rate ( $u_x$  is the velocity in the bulk flow direction and  $z$  is in the depthwise direction) and  $S_i$  is the segregation length scale, which characterizes the segregation propensity of a bidisperse mixture of particles. The segregation length scale for spherical particle diameter ratios from  $1/3 < R < 3$  and density ratios from  $1/10 < R < 10$  is well approximated by

$$S_i/d_s = C \ln(R), \quad (3)$$

where  $d_s$  is the diameter of the smaller species for size-bidisperse mixtures and the diameter for density-bidisperse mixtures, and  $C$  is a constant [14,15].

The segregation continuum model of Eqs. (1)–(3), while developed using bounded heap flows [13,14], is applicable to a wide range of flow geometries [2], including rotating tumblers [12,17], chutes [18], wedge-shaped heaps [19], confined shear flows [20,21], and even more complicated geometries such as hoppers [17,22,23]. Extensions of this bidisperse segregation model, i.e., Eqs. (1)–(3), accurately predict multi- and polydisperse flows of spherical particles [18,24–26] and, with minor modification, flows of spherical particles with high overburden pressure [21]. We note that the linear dependence of the segregation velocity on concentration for spherical particles [Eq. (2)] was developed for mixtures with similar species concentrations [13,14] but is more accurately described for mixtures with widely varying species concentrations by a segregation

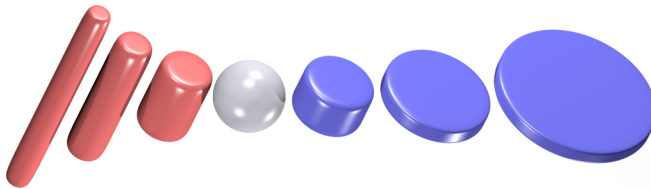


FIG. 1. Depiction of the range of cylindrical and spherical particles sizes. The leftmost particle has length-to-diameter ratio of 9 (rodlike), and the rightmost particle has a length-to-diameter ratio of  $1/9$  (disklike).

velocity model that is quadratic in concentration [27,28]. However, this greater level of fidelity is unnecessary for most mixtures and flow conditions.

The primary goal of this study is to find a relation for the segregation velocity and its key parameters for nonspherical particles that is analogous to Eqs. (2) and (3) for spherical particles, expanding on the results of our short preliminary paper on this topic [29]. The wide range of possible particle shapes makes the search for an appropriate model describing the dependence on local conditions such as shear rate,  $\dot{\gamma}$ , and concentration,  $c_i$ , challenging. Ideally, the model would be similar to Eq. (2), although this model is based on kinetic sieving of spherical particles [16], an approach that may not work as well for the infinitely large parameter space describing nonspherical particles. Even if a model like Eq. (2) can be identified, an even more difficult problem is finding the appropriate parameter (or parameters) analogous to  $S_i$  in Eq. (2) that characterizes segregation between two species of nonspherical particles. Ideally,  $S_i$  for a pair of nonspherical particle species would be a function of a single easily quantifiable ratio, similar to the size or density ratio for spherical particles. However, there is a wide range of parameters upon which the segregation could depend, including the shape factor (a measure of spherical equivalence), a characteristic length scale or scales, the particle volume, or other particle characteristics, noting that in addition to size and volume, a particle's shape can also be described by sphericity, corner roundness, and surface texture [30,31]. Considering the wide range of particles shapes that are possible, it seems unlikely that a single ratio could effectively describe the segregation properties of particles that could vary as widely as those shown in Fig. 1. The objective of this paper, therefore, is to establish a general expression for the segregation velocity analogous to Eq. (2) and to develop an approach for determining the dependence of a parameter like  $S_i$  on the appropriate size and shape characteristics of nonspherical particles analogous to Eq. (3), further extending and explaining our initial results on this subject [29].

As a proxy for mixtures of arbitrary nonspherical particles, we consider millimeter-sized cylindrical particles (rodlike and disklike) as well as spherical particles. Cylindrical particles are used because they are described by just two characteristic lengths, the diameter,  $d$ , and the axial length,  $l$ , and yet can vary substantially in shape, as shown in Fig. 1. To characterize the propensity of a particle mixture to segregate, we measure the segregation velocity  $w_{p,i}$  for a wide range of bidisperse mixtures of cylinders mixed with either other cylinders or with spheres to find an expression for  $w_{p,i}$  that is analogous to Eq. (2) for spherical particles. We then seek a universal parameter or parameters analogous to  $S_i$  [Eq. (3)] for spherical particles based on arbitrary particle size and shape differences that characterize the propensity for segregation of nonspherical particles. The challenge in doing this is to represent the character and degree of segregation over a broad multidimensional shape space, even for cylindrical particles, in a relatively simple form.

## II. SUPERELLIPSOID DEM SIMULATIONS

To investigate segregation of nonspherical particles, we conduct DEM simulations [32–36] of bidisperse particles in a gravity-driven free-surface flow. Although there are many approaches to simulating cylindrical particles [37–41], we use superellipsoid particles [7,8,11,38,42–48]. The

particle shape is based on the inside-outside function for superellipsoids [49],

$$P(\mathbf{X}) = \left( \left| \frac{x}{a} \right|^s + \left| \frac{y}{b} \right|^s \right)^{t/s} + \left| \frac{z}{c} \right|^t - 1, \quad (4)$$

where  $P(\mathbf{X}) = 0$  defines the particle surface. Negative and positive values of  $P(\mathbf{X})$  correspond to the interior and exterior of the particle, respectively. The radii  $a$ ,  $b$ , and  $c$  control the particle length along the  $x$ ,  $y$ , and  $z$  axis, respectively, and parameters  $s$  and  $t$  control corner sharpness in the  $xy$  plane and normal to it, respectively, as well as particle shape. Different values of  $s$  and  $t$  generate different shapes ranging from an octahedron ( $s = 1, t = 1$ ), to a sphere ( $s = 2, t = 2$ ), to cylinderlike ( $s = 2, t \geq 8$ ), to cuboids ( $s \geq 8, t \geq 8$ ). Particles with either  $s < 1$  or  $t < 1$  are concave [49] and are not considered here as they are incompatible with the contact detection algorithm we use, which is described below.

For this study we use spherical particles with  $s = 2$  and  $t = 2$  and cylindrical particles with  $s = 2$  and  $t = 8$ . Increasing  $t$  creates a sharper edge on cylindrical particles. However, values of  $t > 8$  significantly increase simulation time but do not significantly affect the segregation characteristics [38]. We consider mixtures of cylindrical particles with varying diameter ratios,  $R_D$ , and length ratios,  $R_L$ . For mixtures of cylinders and spheres we use the diameter ratio and a modified length ratio,  $R_{L'} = l/d$ , where  $l$  is the cylinder length and  $d$  is the sphere diameter. The range of particle shapes examined in this study is illustrated in Fig. 1, which shows red rodlike and blue disklike particles with maximum and minimum aspect ratios (length to diameter) of 9 and 1/9, respectively. Also shown is a sphere sized relative to the cylindrical particles to illustrate the range of sizes of cylindrical particles used for mixtures of cylindrical and spherical particles. Analytic expressions for the volume and the moments of inertia of the superellipsoid particles used in the simulations and for analysis can be found elsewhere, e.g., Refs. [50,51].

Critical to the accuracy of DEM, regardless of particle shape, is resolving particle contacts. The methodology implemented here uses the greatest overlap of the contacting particle pair to calculate the contact force vector, similar to DEM for spheres. For nonspherical particles represented by the continuous inside-outside function  $P(\mathbf{X})$ ,  $P(\mathbf{X}) < 1$  represents the interior of the particle,  $P(\mathbf{X}) > 1$  represents the exterior of the particle, and  $P(\mathbf{X}) = 1$  represents the particle surface. The points generating the greatest overlap of particles  $i$  and  $j$ ,  $\mathbf{X}_i^c$  and  $\mathbf{X}_j^c$ , respectively, are found by independently minimizing the Lagrangian optimization problems [52,53]:

$$\begin{aligned} \Pi_i &= P_j(\mathbf{X}_i^c) - \lambda_i P_i(\mathbf{X}_i^c), \\ \Pi_j &= P_i(\mathbf{X}_j^c) - \lambda_j P_j(\mathbf{X}_j^c). \end{aligned} \quad (5)$$

The contact detection algorithm is applicable to any  $P(\mathbf{X})$  that is twice differentiable, which is the case for the superellipsoid particles used here [45,54]. To reduce the number of times the contact algorithm is applied to noncontacting particles, contact screening algorithms of spatial hashing, bounding sphere contact evaluation, and object oriented bounding box contact detection are used [11,38].

Simulations are performed using an in-house DEM code on NVIDIA GTX Titan X GPUs installed in a workstation computer running Ubuntu 14.04 LTS. Earlier versions of this code were validated against experimental data from millimeter-sized spherical glass, ceramic, and steel particles in bounded heap flows of size and density bidisperse flows [15,19–22,28]. Validation for nonspherical particles is described below. Similar to DEM simulations of spherical glass particles, the forces between contacting superellipsoid particles  $i$  and  $j$  are modeled using a contact-only repulsive spring-dashpot model [32] for the normal force,  $\mathbf{F}_{ij}^n = -k_n \sigma_{ij} - 2\zeta_n m_{\text{eff}} \mathbf{v}_{ij}^n$ , where the normal stiffness,  $k_n = (\pi/t_c)^2 + \zeta_n^2$ , and normal damping,  $\zeta_n = -\ln e/t_c$  [34], parameters are determined by the restitution coefficient,  $e = 0.8$ , and the binary collision time,  $t_c = 10^{-3}$  s (which is small enough to accurately model gravity driven flow of glass particles [13,35]),  $\sigma_{ij}$  is the directed particle overlap at the contact,  $m_{\text{eff}} = m_i m_j / (m_i + m_j)$  is the effective mass, and  $\mathbf{v}_{ij}^n$  is the relative normal velocity at the contact point. The tangential contact force,  $\mathbf{F}_{ij}^t =$

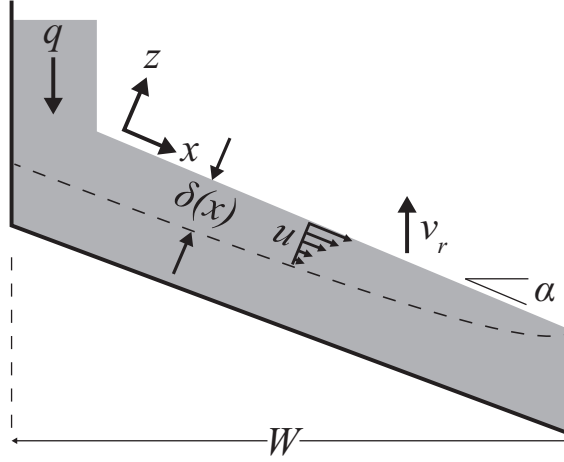


FIG. 2. Schematic of the 2D bounded heap with periodic spanwise boundary conditions in the  $T$ -wide  $y$  direction. The coordinate system is rotated by the repose angle  $\alpha$  and rises at the heap-rise velocity  $v_r$ . The flowing layer shape is idealized, and its thickness is exaggerated for purposes of illustration.

$\min(\mu \|\mathbf{F}_{ij}^n\|, \|k_t \Sigma(\mathbf{v}_{ij}^t \Delta t) - 2\zeta_t m_{\text{eff}} \mathbf{v}_{ij}^t\|) \mathbf{v}_{ij}^t / \|\mathbf{v}_{ij}^t\|$ , is the minimum of the Coulomb friction for sliding contacts and the tangential spring-dashpot force (to emulate static friction) where  $k_t = 2k_n/7$  and  $\zeta_t = 2\zeta_n/7$  are the tangential stiffness and damping coefficients, respectively [34],  $\mathbf{v}_{ij}^t$  is the relative tangential velocity at the contact, and  $\Delta t = t_c/40 = 2.5 \times 10^{-5}$  s is the simulation time step [36]. Particle-particle and particle-wall contacts both use a friction coefficient of  $\mu = 0.4$ .

### III. SIMULATIONS AND VALIDATION

Simulations of a single-sided, quasi-2D bounded heap, shown schematically in Fig. 2, are performed by vertically feeding an equal volume mixture of two particle species on one side of a box (rectangular prism) with, except for validation simulations, a spanwise extent  $T/l_{\text{max}} = 8$  and width  $W/l_{\text{max}} = 200$ , where  $l_{\text{max}}$  is the diameter of the minimum bounding sphere of the larger particle species. For superellipsoids,  $l_{\text{max}} = 2\sqrt{a^2 + c^2}$ . We study segregation in the steady state where the heap spans the full width of the box, and particles flow in a thin “flowing layer” down the surface of the heap toward the wall opposite the feed zone. The flowing layer (region above the dashed line in the figure) has thickness  $\delta$ . The geometry is periodic in the spanwise ( $y$ -) direction, unless indicated otherwise, to avoid sidewall effects. The bottom bounding wall has a no-slip surface (i.e., particles contacting it are immobilized) and a slope ( $30^\circ$ ) approximately equal to the heap repose angle,  $\alpha$ , to reduce the total number of particles needed in the simulation. Particles fall onto the heap at a 2D feed rate,  $q = Q/T$ , where  $Q$  is the volumetric flow rate. Particles are continuously deposited onto the “static” heap from the bottom of the flowing layer. A steady-state flow is reached after the depth of the flowing layer,  $\delta$ , is greater than the depth of the heap, and the surface of the heap rises at a steady rise velocity,  $v_r = q/W$ . The coordinate system is at the upstream end of the flowing layer and oriented with the  $x$  axis parallel to the free surface, the  $y$  axis in the spanwise direction, and the  $z$  axis normal to the free surface. The coordinate system also rises at  $v_r$ , so in its frame of reference the flow and segregation are steady.

The DEM simulations for superellipsoid cylindrical particles are validated by comparing the average species concentration deposited on the fixed bed below the flowing layer to experiments with cylindrical nylon particles (E&T Fasteners, CA, USA) with dimensions given in Table I and physical properties of density  $\rho = 1.15$  g/cm<sup>3</sup> and friction coefficient  $\mu = 0.5$  [55]. The particles are dyed different colors using Rit DyeMore synthetic fabric dye so that they can be

TABLE I. Measured cylinder dimensions (dimensions used in validation simulations).

Particle	Diameter (mm) +/- 0.1	Length (mm) +/- 0.4
<i>D1</i>	6.3 (6.350)	3.2 (3.175)
<i>R1</i>	3.2 (3.175)	4.7 (4.750)
<i>R2</i>	3.2 (3.175)	12.7 (12.700)
<i>R3</i>	6.3 (6.350)	9.5 (9.525)

easily distinguished. An equal volume mixture of bidisperse particles are fed by an auger feeder (Acrison, Inc., NJ, USA) onto the experimental quasi-2D bounded heap as described previously [56]. The apparatus has a spanwise gap  $T = 3.8$  cm between two glass plates, width  $W = 61$  cm, and a depth of 91 cm. Like the DEM simulations, a sloped lower boundary reduces the number of particles required for the experiments. Two experiments are performed for each of the three cases specified in Table II, and average results are reported. Validation simulations only use  $e = 0.5$  to determine particle stiffness and damping coefficients. The dimensions of the simulated particles are the nominal manufacturer-specified values given in parentheses in Table I.

The deposited concentration is measured at the wall for both the experiments and the corresponding DEM simulations. To ensure an accurate comparison, DEM simulations are performed in a heap with geometry identical to the experimental apparatus, including planar, frictional sidewalls rather than the periodic boundaries used for all other simulations. To quantify segregation, a digital photograph of the side of the heap is used for the experiments and a POV-RAY [57] rendering of the side of the heap is used for the simulations. The final state of the heap in experiment and simulation for validation case 1 is shown in Fig. 3. The rodlike red particles (*R1*) deposit upstream in the heap, and the disklike blue particles (*D1*) deposit closer to the downstream end wall. For each validation case, the deposited concentration is calculated from the image (for experiment) or rendering (for simulation) in the region between the parallel green lines in Fig. 3. Particles above the upper green line are excluded because their distribution reflects the transient deposition of particles that occurs after the feed stops, and particles below the lower green line are excluded because they are deposited before the deposition of particles on the heap becomes steady. The length of the heap is split into 50 bins, each spanning the height of the evaluation area. The particle species represented by each pixel is determined by comparing the dot product of the RGB vector of the pixel and a reference value for the color of each species. The concentration of the two particle species at the wall is determined by simply counting pixels associated with each species.

For each validation case, the deposited streamwise concentration profile of disklike particles (*D1*) averaged across two experiments and from one simulation are shown in Fig. 4. The results demonstrate that the DEM simulations capture the deposited particle concentration for the case of frictional sidewalls. We therefore infer that the DEM simulations also correctly capture the segregation behavior of superellipsoid particles for the periodic boundary case, which is used for the remaining results to avoid ordering effects related to particles aligning to the sidewall [11], see Sec. V.

TABLE II. Cases for DEM simulation validation (ratios from simulations).

Case	Particles	$R_D$	$R_L$	$R_V$	$q$ (cm <sup>2</sup> /s)	$T/l_{\max}$	$W/l_{\max}$
1	<i>D1, R1</i>	0.5	1.5	0.4	26.3	5.4	85.9
2	<i>D1, R2</i>	0.5	4.0	1.0	22.7	2.9	46.6
3	<i>D1, R3</i>	1.0	3.0	3.0	22.7	3.3	53.3

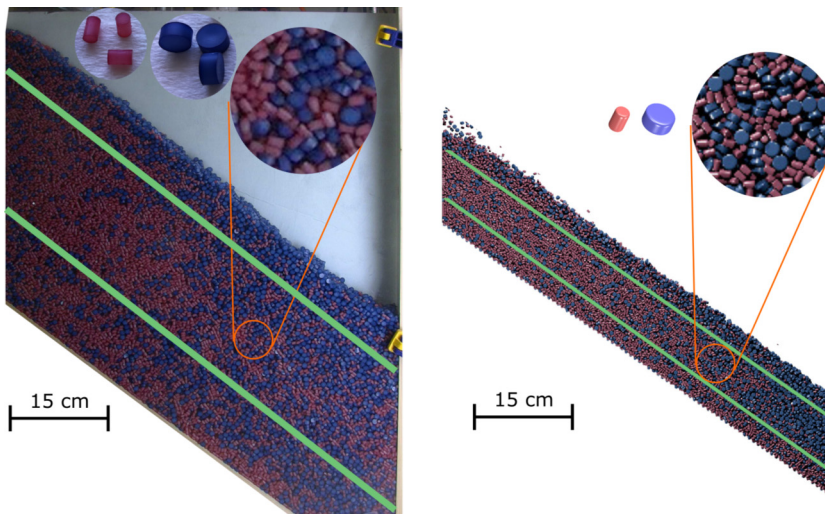


FIG. 3. Heap segregation in experiment (left) and simulation (right) for validation case 1 (see Table II) with blue disklike ( $d = 6.3$  mm,  $l = 3.2$  mm) and red rodlike ( $d = 3.2$  mm,  $l = 4.7$  mm) cylinders. Example particles and a magnified section of the sidewall are shown above each heap image. Average deposited streamwise concentration profiles are calculated in the region between the two green lines.

#### IV. SEGREGATION IN BIDISPERSE MIXTURES OF CYLINDRICAL PARTICLES

To quantify the segregation, the results from each simulation are spatially and temporally averaged to find the bulk and species velocity,  $\mathbf{u}$  and  $\mathbf{u}_i$ , respectively, the segregation velocity  $w_{p,i}$ , and species concentration  $c_i$ , throughout the flowing layer, as in previous studies [12,14,15,25,28]. For each output time step, quadrilateral bins oriented parallel to and rising with the free surface are used to average DEM simulation data. Bin dimensions are  $l_{\max}/2$  in the depthwise direction,  $2l_{\max}$  in the streamwise direction, and  $T$  in the spanwise direction. Within each bin, flow kinematics and species concentrations are averaged over all output time steps, noting that the bins remain fixed relative to the surface of the flowing layer since their boundaries are defined with respect to the rising reference frame. Particles overlapping multiple bins have their weighted partial volume applied to each overlapped bin. The concentration of species  $i$ ,  $c_i$ , in a bin is defined as

$$c_i = \frac{\sum V_{i,j}}{V_{\text{bin}}}, \quad (6)$$

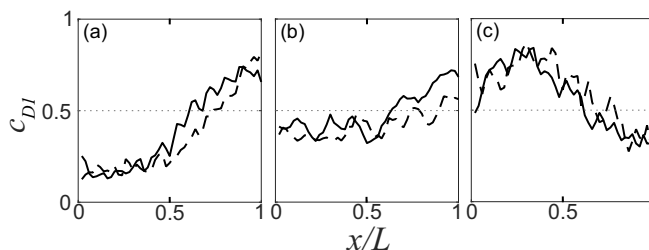


FIG. 4. Deposited concentration at the wall of disklike particles  $D1$  ( $d = 6.3$  mm,  $l = 3.2$  mm) for equal volume concentration mixtures with three different rodlike particles from experiment (solid) and DEM simulation (dashed) for validation cases (a) 1, (b) 2, and (c) 3, see Table II. The deposited concentration for the example in Fig. 3 is shown in (a).

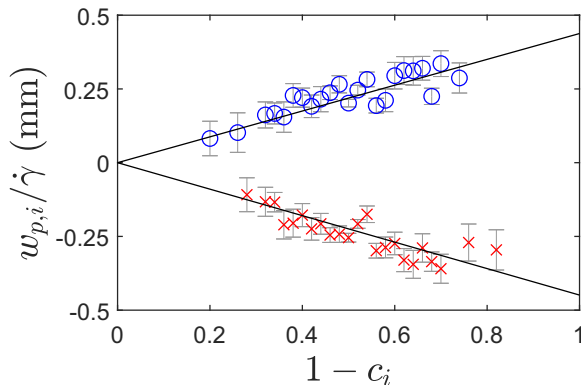


FIG. 5. Segregation velocity,  $w_{p,i}/\dot{\gamma}$ , vs  $1 - c_i$  from DEM simulation for  $d = 6.35$  mm and  $l = 3.175$  mm cylinders (blue  $\circ$ ) and  $d = 3.175$  mm and  $l = 4.75$  mm cylinders (red  $\times$ ) for validation case 1, but with periodic instead of frictional sidewalls. Linear least-squares fits to Eq. (2) (lines) provide a segregation length scale value of  $|S_i| = 0.44$  mm. Data averaged into 0.02-wide concentration bins.

where  $V_{i,j}$  is the partial volume of particle  $j$  of species  $i$  and  $V_{\text{bin}}$  is the total volume of all particles in the bin. The mean velocity of species  $i$  in a bin  $\mathbf{u}_i$  is volume weighted as

$$\mathbf{u}_i = \frac{\sum \mathbf{u}_{i,j} V_{i,j}}{\sum V_{i,j}}, \quad (7)$$

where  $\mathbf{u}_{i,j}$  is the velocity of particle  $j$  of species  $i$ . The shear rate in a bin is calculated from the streamwise velocity component as

$$\dot{\gamma} = \frac{\Delta u}{\Delta z}, \quad (8)$$

where  $\Delta u$  is the difference in the mean bin velocity between the target bin and the bin below it divided by the bin height  $\Delta z$ . The local segregation velocity  $w_{p,i}$  for each species  $i$  in each bin in the flowing layer is calculated as

$$w_{p,i} = w_i - w, \quad (9)$$

where  $w_i$  is the mean species velocity and  $w$  is the mean velocity of all particles in the bin. We note that the specific details of how the concentration and kinematic quantities are obtained are not critical. In fact, we would expect that results obtained using the binning method described here would be similar to those that would be obtained using coarse-graining methods [58]. We further note that diffusion plays a small role in calculating the segregation velocity and can be safely ignored here [28].

### A. Segregation dependence on shear rate and concentration

We first investigate the dependence of segregation velocity on  $\dot{\gamma}$  and  $c_i$  for mixtures of cylinders. Figure 5 shows an example of the segregation velocity, scaled by  $\dot{\gamma}$  as in previous studies [14,28], vs concentration for a bidisperse mixture of  $d = 3.2$  mm and  $l = 4.7$  mm cylinders (*R1*) and  $d = 6.3$  mm and  $l = 3.2$  mm cylinders (*D1*), the same particles from validation case 1, for a simulation with periodic sidewall boundary conditions. The data fall along two lines, one for each of the species, that both go to zero at  $1 - c_i = 0$ . This result is consistent with Eq. (2) where the segregation length scale  $S_i$  is the slope from the linear least-squares fit of the data forced through (0,0), consistent with the result for size bidisperse and density bidisperse spherical particles [14,15]. Note that the data include time-averaged values for  $w_{p,i}/\dot{\gamma}$  vs  $1 - c_i$  through the entire flowing



layer (all bins) during the steady filling (and segregation) associated with bounded heap flow. In general, this data captures a wide range of values for  $w_{p,i}$ ,  $\dot{\gamma}$ , and  $c_i$  because data are obtained at different locations in the flowing layer. For the larger volume cylinders ( $D1$ ),  $w_{p,i}$  and  $S_i$  are both positive, indicating that they rise in the flowing layer, while for the smaller cylinders ( $R1$ ),  $w_{p,i}$  and  $S_i$  are negative, indicating that they sink in the flowing layer. This segregation drives large cylinders toward the surface of the flowing layer where they are advected to the downstream portion of the heap nearer the right wall, while small cylinders sink in the flowing layer and are deposited further upstream on the heap. This is consistent with the results shown in Figs. 3 and 4(a), although the segregation data in Fig. 5 are for periodic rather than frictional sidewall boundaries.

Similar results to those shown in Fig. 5 are found for all other particle mixtures considered here, thereby demonstrating the validity of Eq. (2) for nonspherical particles as well as spherical particles. This result is somewhat surprising, given that Eq. (2) is based on a simplification of a kinetic sieving model for spherical particles [16]. On the other hand, it is reasonable that  $w_{p,i}$  depends on the shear rate, since relative motion of particles is necessary for segregation to occur, and the concentration of the other particle species  $1 - c_i$ , since particles will only segregate if they interact with particles of the other species.

With the understanding that Eq. (2) is valid for mixtures of cylindrical particles as well as spherical particles, the challenge now is to understand the dependence of  $S_i$  on particle shape. Previous studies have shown that normalizing  $S_i$  by a relevant particle length scale (the small particle diameter  $d_s$  for mixtures of spheres) allows  $S_i$  to be represented solely as a function of a relevant ratio of a particle property, such as the diameter or density ratio for spheres as indicated in Eq. (3) [14,15,28]. For nonspherical particles, the appropriate length scale to nondimensionalize  $S_i$  is not obvious, although, like spherical particles, we would expect it to be on the order of the particle size (as opposed to a length scale based on the dimensions of the experimental apparatus). For cylindrical particles, candidate length scales include the diameter, length, diameter of a bounding sphere, and diameter of an equal volume sphere. Of these, only the diameter of a bounding sphere and the diameter of an equal volume sphere generalize to arbitrary particle shape. Although there is no clear physical basis for which of the two to select, we use the diameter of the volume-equivalent sphere of the smaller volume species,  $d_{s,eq} = 2[3V_s/(4\pi)]^{1/3}$ , where  $V_s$  is the volume of the smaller species, as the characteristic particle length scale. Using any of the other characteristic particle length scales does not improve, and in some cases greatly diminishes, the collapse of the data for the results discussed below.

## B. Cylindrical particle mixtures

With this background in place, we now consider the segregation, characterized by  $S_i/d_{s,eq}$ , of bidisperse mixtures for a broad range of species  $A$  cylindrical particles and species  $B$  cylindrical particles. First, we examine the dependence of  $S_i/d_{s,eq}$  on the length ratio,  $R_L = l_A/l_B$ , and the diameter ratio,  $R_D = d_A/d_B$ . Figure 6 shows  $S_i/d_{s,eq}$  for 63 simulations in which the diameter of particle species  $A$  equals the length of particle species  $B$ , i.e.,  $d_A = l_B$ , for the reference particles of a monodisperse mixture. We define  $R_* = l_B/d_A$  as the reference ratio, which corresponds to the aspect ratio of the monodisperse mixture when  $R_L = R_D = 1$ . In Fig. 6,  $R_* = 1$  and the corresponding monodisperse mixture corresponds to a cylinder with diameter equal to its length (lower-right corner of the figure). The length ratio,  $R_L = l_A/l_B$ , is varied by increasing  $l_A$ , and the diameter ratio,  $R_D = d_A/d_B$ , is varied by increasing  $d_B$ . Moving up in the figure from the monodisperse mixture at the lower right corner corresponds to  $A$  particles (shown in red) becoming longer (more rodlike), while moving left corresponds to  $B$  particles (shown in blue) increasing in diameter (more disklike). The upper-left corner of the figure corresponds to rodlike  $A$  particles and disklike  $B$  particles. The symbol diameter in Fig. 6 is proportional to the magnitude of the segregation length scale for  $A$  particles,  $S_A/d_{s,eq}$ , and colors are interpolated from the data points. The segregation length scale of species  $B$ , which is not shown, is negative and nearly equal in magnitude to  $S_A$  with an average rms deviation from  $S_A$  of 7% across all 63 measurements.

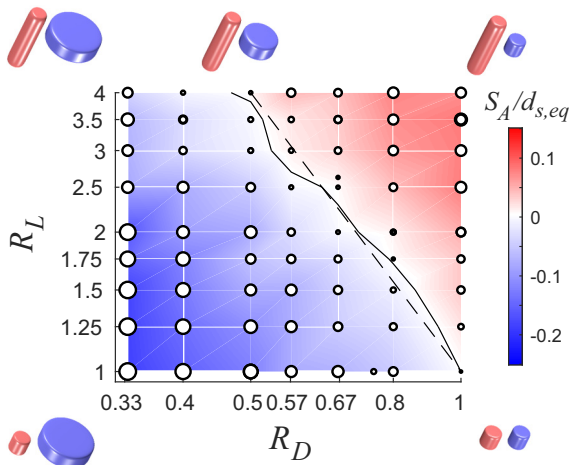


FIG. 6. Nondimensional segregation length scale of the longer species  $A$ ,  $S_A/d_{s,eq}$ , vs length ratio  $R_L$  and diameter ratio  $R_D$  for  $R_* = 1$ . Data symbol ( $\circ$ ) diameter is proportional to  $S_A/d_{s,eq}$ , and color contours are interpolated from data points. The zero segregation contour ( $S = 0$ , black curve) corresponds closely to an equal volume ratio,  $R_V = 1$  (dashed line). Representative particles of species  $A$  (red) and species  $B$  (blue) are shown at each corner and the top of the equal-volume line.

Figure 6 shows that longer cylinders rise in the presence of shorter cylinders (upper right), corresponding to  $S_A/d_{s,eq} > 0$ , and larger diameter cylinders rise in the presence of smaller diameter cylinders (lower left), corresponding to  $S_A/d_{s,eq} < 0$ . Furthermore, segregation is strongest when the volume of the two particles differs substantially at the upper-right and lower-left corners. Between these two extremes is a region where the particles do not segregate ( $S_A = S_B = 0$ ) and, consequently, remain mixed. The corresponding contour (solid black curve) extends, as expected, through  $R_D = R_L = 1$  for a monodisperse (uniform) “reference mixture” at the lower-right corner. This suggests that the relative volumes of particles  $A$  and  $B$  might determine the degree of segregation. To test this hypothesis, we plot an equal volume ratio,  $R_V = V_A/V_B = 1$ , line (dashed) in Fig. 6. This line closely follows the  $S_A = S_B = 0$  zero-segregation contour, confirming that particles having similar volume remain mixed for this range of  $R_D$  and  $R_L$ , and for  $R_* = 1$ . Particles with equal volumes are shown at the top end of the dashed line to demonstrate how different the particle shapes can be that remain mixed.

The dependence of segregation on the relative volumes of the two particle species can be further explored by changing the reference ratio  $R_*$ . The variable space explored is shown in Fig. 7 for  $1 < R_L < 4$ ,  $1/3 < R_D < 1$ , and  $1/3 < R_* < 3$ , where Fig. 6 corresponds to the red plane at  $R_* = 1$ . Each symbol in Fig. 7 represents a simulation for which the segregation length scale is measured (325 total DEM simulations).

To explore this parameter space further, we conduct simulations in additional planes of the variable space. First, consider planes analogous to that in Fig. 6 for  $R_* = 1$  but instead for  $R_* = 1/3$  and  $R_* = 3$  (green planes in Fig. 7). Figure 8(a) for  $R_* = 1/3$  corresponds to mixtures of disklike cylinders with a monodisperse pair at the lower-right corner of the figure. Moving up in the figure increases the length of particle  $A$  (red particles) so that by the top of the figure its length is  $4/3$  its diameter. Moving left in the figure results in a larger diameter for particle  $B$  (blue). Thus most of the particles considered here (except red  $A$  particles for  $R_L > 3$ ) are disklike. Again, it is evident that mixtures with particles having larger differences in volume tend to segregate more, whether it is longer particles in the upper-right or larger diameter disks in the lower left. Also evident is that the solid contour for  $S_A = 0$  is well approximated by the dashed line corresponding to equal volume particles.

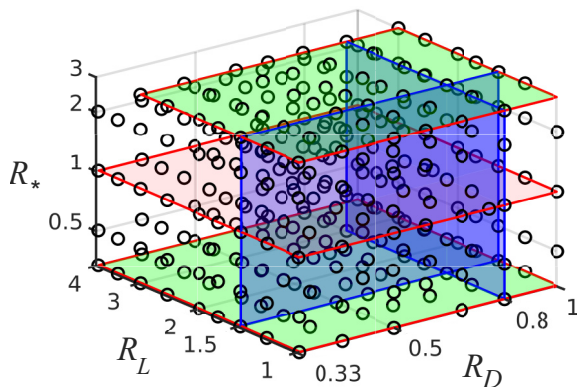


FIG. 7.  $R_D$ ,  $R_L$ , and  $R_*$  parameter space for mixtures of cylindrical particles where each circle represents one of the 325 simulations performed. Colored constant-ratio planes correspond to data shown in Fig. 6 (red), Fig. 8 (green), and Fig. 9 (blue).

Figure 8(b) for  $R_* = 3$  corresponds to monodisperse mixtures of rodlike cylinders. Moving up in the figure from the monodisperse mixture at  $R_L = R_D = 1$  increases the length of particle A (red), making it even longer, while moving left in the figure results in a larger diameter particle B (blue), though its length remains longer than its diameter. Hence, this figure represents mixtures of rods. Like the previous two cases, mixtures with particles having a larger volume difference segregate more (upper right and lower left), and the solid contour for  $S_A = 0$  nearly overlays the dashed line for equal volume particles. Again, particles at the top end of the dashed line in Figs. 8(a) and 8(b) demonstrate how much the particles that remain mixed can differ in shape.

A different perspective can be obtained by considering values for  $S_i/d_{s,eq}$  in the  $R_*-R_D$  plane at  $R_L = 1.5$  and in the  $R_*-R_L$  plane at  $R_D = 0.8$  (blue planes in Fig. 7), shown in Fig. 9. The lower-left corner of both figures corresponds to a reference ratio that is more disklike. Moving right in either figure changes the reference particle from disklike to having an equal length and diameter in the middle ( $R_* = 1$ ) to more rodlike on the right side of the figure. At the bottom of Fig. 9(a), particle

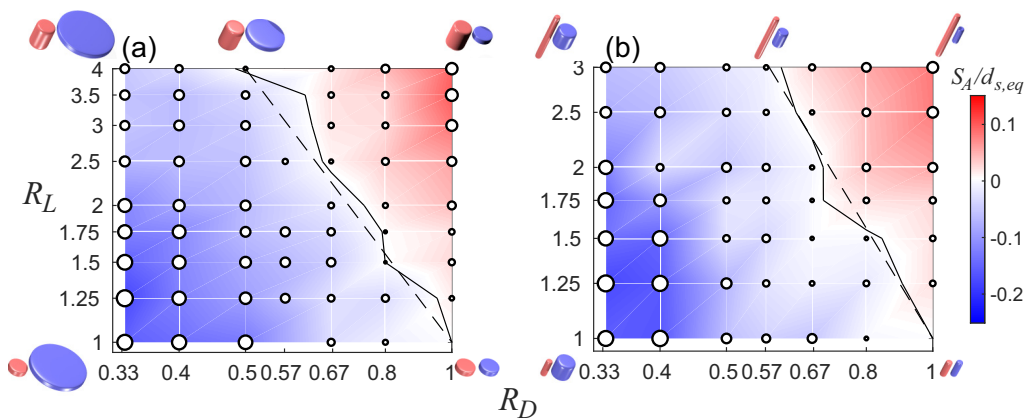


FIG. 8. Dependence of  $S_A/d_{s,eq}$  on  $R_L$  and  $R_D$  for (a)  $R_* = 1/3$  and (b)  $R_* = 3$  (green planes in Fig. 7). Symbol (o) diameter is proportional to  $S_A/d_{s,eq}$ , and color contours are interpolated from data points. The zero segregation contour ( $S = 0$ , black curve) again (as in Fig. 6) corresponds closely to an equal volume ratio,  $R_V = 1$  (dashed line). Representative particles of species A (red) and species B (blue) are shown at each corner and the top of the equal-volume line.

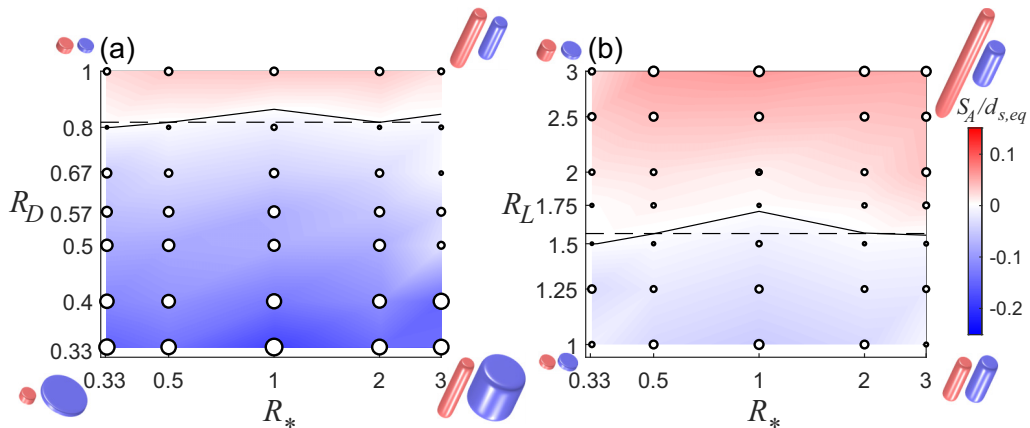


FIG. 9. Dependence of  $S_A/d_{s,eq}$  on (a)  $R_*$  and  $R_D$  for  $R_L = 1.5$  and (b)  $R_*$  and  $R_L$  for  $R_D = 0.8$  (blue planes in Fig. 7). Symbol ( $\circ$ ) diameter is proportional to  $S_A/d_{s,eq}$ , and color contours are interpolated from data points. The zero segregation contour ( $S = 0$ , black curve) again (as in Figs. 6 and 8) corresponds closely to an equal volume ratio,  $R_V = 1$  (dashed line). Representative particles of species A (red) and species B (blue) are shown at each corner.

species B (blue) has a much larger diameter than species A (red), and moving up decreases the diameter of species B until it equals the diameter of species A at the top of the figure. In Fig. 9(b), moving up from the bottom of the figure increases the length of species A (red). In both figures, the solid black contour for  $S_A/d_{s,eq} = 0$  is nearly identical to the dashed line for equal volume particles. The figures also demonstrate that  $R_*$  has little effect on  $S_A/d_{s,eq}$  and that the variation in magnitude of  $S_A/d_{s,eq}$  with changing  $R_D$  is greater than the variation of  $S_A/d_{s,eq}$  with  $R_L$  (in both cases the ratio plotted on the vertical axis changes by a factor of 3). This is because the volume of cylindrical particles depends quadratically on diameter but only linearly on length, resulting in a much larger change in particle volume for the range of  $R_D$  in the left figure than for the range of  $R_L$  in the right figure.

The close correspondence of the equal volume ratio line and the  $S_A = 0$  contours in Figs. 6, 8, and 9, and the related observation that larger volume particles always segregate upward while smaller volume particles sink downward strongly suggests that the scaled segregation length scale,  $S_i/d_{s,eq}$ , depends on the volume ratio  $R_V = V_A/V_B$ . To test this hypothesis, Fig. 10 plots  $S_i/d_{s,eq}$  vs  $R_V$  for 325 simulations for all of the parameter combinations shown in Fig. 7. Note that there are two data points for each simulation: one is for species A at a particular value of  $R_V$  and another for species B at  $1/R_V$ . Since there are so many data points, they are rendered semitransparent so overlapping points are more intense in color. The segregation measured in terms of  $S_i/d_{s,eq}$  is, to first order, linear with  $\ln(R_V)$  and follows the same relationship as for spherical particles [Eq. (3)] when the length scale  $d_s$  is replaced by a spherical equivalent length scale for nonspherical particles  $d_{s,eq}$  and the diameter ratio is replaced by the volume ratio, which is shape independent. Thus,

$$S_i/d_{s,eq} = C_* \ln(R_V). \quad (10)$$

For cylindrical particles, Eq. (10) has a slope corresponding to  $C_C = 0.080 \pm 0.004$  (95% confidence interval), where the subscript C corresponds to mixtures of cylindrical particles. While there is some scatter in Fig. 10, it is remarkable that the segregation of cylindrical particles varying so widely in shape and size, i.e., spanning the range shown in Fig. 1 for rods and disks, can be condensed to this simple correlation.

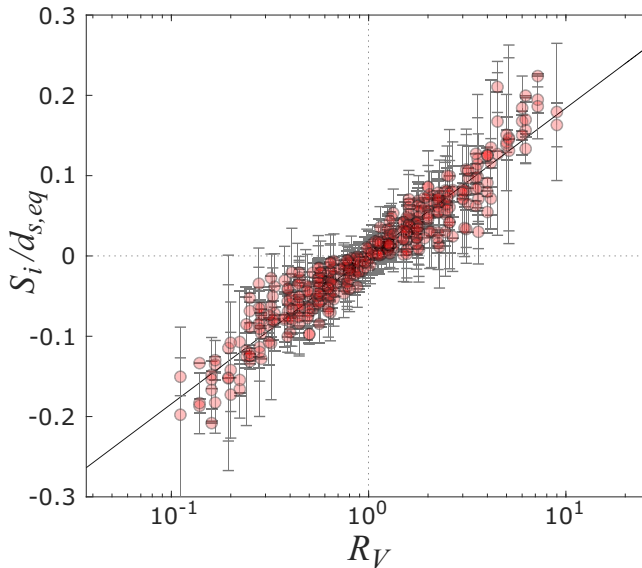


FIG. 10. Scaled segregation length scale,  $S_i/d_{s,eq}$ , vs volume ratio  $R_V$  for data from simulations with cylindrical species mixtures indicated in Fig. 7. Symbols are semitransparent, so regions with overlapping symbols are more intense in color. Error bars correspond to the rms deviation of the fit for  $S_i/d_{s,eq}$  in Eq. (2). Slope of linear least-squares fit to Eq. (10) (line) is  $C_C = 0.080$ .

### C. Mixtures of cylindrical and spherical particles

To further test the dependence of segregation on volume ratio for two particle species, we also conduct DEM simulations for mixtures of cylindrical particles and spherical particles to determine the corresponding values of  $S_i/d_{s,eq}$ . Results are shown in Fig. 11(a) for 54 simulations of bidisperse mixtures of cylinders (species A) and spheres (species B) spanning diameter ratio  $1/2 \leq R_D = d_A/d_B \leq 2$  and length to diameter ratio  $1/2 \leq R_L = l_A/d_B \leq 2$ . The parameter space for bidisperse mixtures of spheres and cylinders, disregarding absolute size, is fully characterized by  $R_L$  and  $R_D$ .

As with mixtures of cylindrical particles, the particle species with the greater volume segregates upward, and the particle species with the smaller volume sinks. And again, the equal volume particle line nearly matches the  $S_A = 0$  contour, indicating that the relative volumes of the cylindrical particle and spherical particle determine the degree of segregation. This is confirmed in Fig. 11(b), which shows that  $S_i/d_{s,eq}$  depends linearly on  $\ln(R_V)$  with a slope for cylinder-sphere mixtures (subscript CS)  $C_{CS} = 0.084 \pm 0.006$ , similar to the result for mixtures of cylinders ( $C_C = 0.080$ ) in Eq. (10).

## V. DISCUSSION

### A. Universal relation for cylindrical and spherical particle mixtures

Data from 325 simulations of bidisperse mixtures of cylinders ( $1 \leq R_L \leq 4$ ,  $1/3 \leq R_D \leq 1$ , and  $1/3 \leq R_* \leq 3$ ) and 54 simulations of bidisperse mixtures of spheres and cylinders ( $1/2 \leq R_L \leq 2$  and  $1/2 \leq R_D \leq 2$ ) provide strong support for our observation that the volume ratio between particle species differing in shape is the primary factor controlling the degree of segregation. This point is further amplified by additionally considering the dependence of  $S_i/d_s$  on  $R_V$  for size-bidisperse mixtures of spheres. Using data from previous work [14] and applying the same

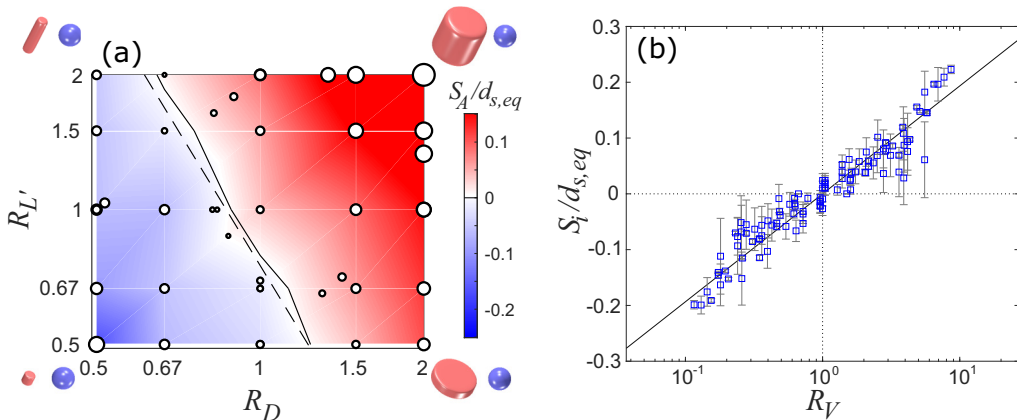


FIG. 11. (a) Nondimensional segregation length scale,  $S_A/d_{s,eq}$ , vs  $R_{L'}$  and  $R_D$  for cylindrical particle (A) in bidisperse mixtures of cylinders and spheres. Symbol ( $\circ$ ) diameter is proportional to  $S_A/d_{s,eq}$ , and color contours are interpolated from data points. The zero segregation contour ( $S = 0$ , black curve) again (as in Figs. 6, 8, and 9) corresponds closely to an equal volume ratio,  $R_V = 1$  (dashed line). Representative particles of species A (cylinders, red) and species B (spheres, blue) are shown at each corner. (b)  $S_i/d_{s,eq}$  vs  $R_V$  for bidisperse mixtures of cylinders and spheres. Error bars correspond to the rms of the fit for  $S_i/d_{s,eq}$  in Eq. (2). Slope of linear least-squares fit to Eq. (10) (line) is  $C_{CS} = 0.084$ , where the subscript CS corresponds to mixtures of cylinders and spheres.

methodology to determine the slope of  $S_i/d_{s,eq}$  vs  $\ln(R_V)$ , we find  $C_S = 0.086 \pm 0.002$  for spherical particle mixtures.

The similarity between the fit coefficients in Eq. (10) as a function of  $R_V$  for mixtures of cylinders ( $C_C = 0.080$ ), cylinders and spheres ( $C_{CS} = 0.084$ ), and spheres ( $C_S = 0.086$ ) suggests that the effect of particle shape on segregation is relatively small compared to volume effects. This conclusion is further supported by Fig. 12, which plots all the data for these three types of mixtures. In addition, we include  $S_i$  data from a previous study of equal diameter rods varying in length in a bounded heap flow with frictional sidewalls [11]. The degree of collapse is remarkable given the range of particle size and shape combinations as well as the different DEM simulation parameters and methods. Fitting the 525 individual simulations in Fig. 12 including the data for mixtures of spherical particles [14], but excluding mixtures of rods with frictional sidewalls [11], to Eq. (10) gives  $C_* = 0.082 \pm 0.003$ . We note that in addition to the volume ratio  $R_V$ , we also considered several other ways to characterize the two particle species, including surface area, projected surface area in the direction of segregation, and sphericity, but none collapse the data better than  $R_V$  for mixtures of cylinders, mixtures of cylinders and spheres, and mixtures of spheres.

The values for  $C_*$  and the associated coefficients of determination  $R^2$  of the fit for each type of particle mixture are provided in the second and third columns of Table III. The fits ( $R^2$ ) for the segregation rate for mixtures of cylinders (C) or mixtures of cylinders and spheres (CS) are not as good as those for spherical particles (S). The increased variability of the segregation rate for nonspherical particles is likely related to the secondary effect of particle shape.

In an attempt to account for the shape effect with the goal of better collapsing the data, we evaluate modifying the particle volume ratio through multiplication or division by other shape characteristics, specifically, the surface area ratio, the ratio projected surface area in the direction of segregation, the sphericity ratio, and the aspect ratio, to determine if including any of these ratios results in a better collapse of the data. Most of these modifications lead to a diminished collapse (smaller  $R^2$ ), except for multiplying by the surface area ratio  $R_{SA}$  or dividing by the sphericity ratio  $R_{Sph}$ , which are both indicated in Table III. However, these both only have a negligible effect on the collapse of the data, as indicated by the coefficients of determination  $R^2$ . From this

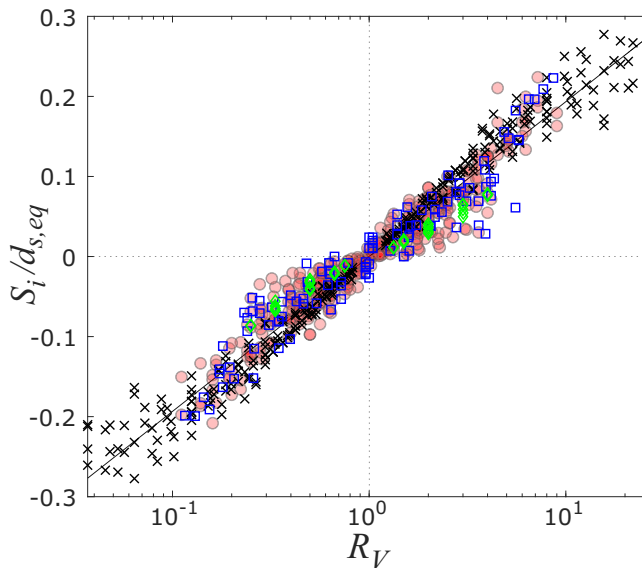


FIG. 12. Nondimensional segregation length scale,  $S_i/d_{s,eq}$ , vs volume ratio  $R_V$  for bidisperse mixtures of cylinders (red  $\circ$ ), cylinders and spheres (blue  $\square$ ), spheres (black  $\times$ ) [14], and cylinders with frictional sidewalls (green  $\diamond$ ) [11]. The linear least-squares fit to the data (line) for all types of mixtures to Eq. (10) has slope  $C_* = 0.082$ .

result, we conclude that of these parameters, volume ratio is the simplest effective parameter to collapse the data. Thus Fig. 12 and Table III demonstrate that, to first order, the segregation of bidisperse mixtures of cylindrical particles or cylindrical and spherical particles in which the particle orientation is relatively stable can be modeled as the segregation of a mixture of volume-equivalent spheres. Furthermore, Eq. (10) can be used as a universal relation to estimate  $S_i/d_{s,eq}$  for spheres, cylinders, and combinations thereof using  $C_* = 0.082$ .

While the dependence of the segregation velocity on the volume ratio is clear, the physics associated with this result is not. The segregation is clearly not a result of the mass difference because the larger volume particle, which segregates upward, has a greater mass. Furthermore, the volume occupied by the larger volume particle has a higher mass density than the same volume occupied by the smaller particle species because of voids between the smaller particles, so this is clearly not a buoyancylike effect. In previous studies of single intruder particle segregation, the volume ratio of a single intruder sphere to a spherical particle in a bed of particles undergoing shear determines the direction of segregation. This reverses from upward to downward at a volume ratio of about 64, so that the large intruder particle sinks as a result of increased weight relative to the

TABLE III. Constant  $C_*$  and coefficient of determination  $R^2$  for Eq. (3) for various mixtures of cylinders (C) and spheres (S).

Mixture	$R_V$		$R_V R_{SA}$		$R_V/R_{Sph}$	
	$C_*$	$R^2$	$C_*$	$R^2$	$C_*$	$R^2$
C	0.080	0.829	0.046	0.831	0.073	0.821
CS	0.084	0.876	0.050	0.871	0.080	0.855
S [14]	0.086	0.975	0.052	0.975	0.086	0.975
All	0.082	0.894	0.050	0.900	0.081	0.898

upward contact forces from the bed of smaller particles [59]. However, this volume ratio (64) is well above the volume ratios considered here.

Further demonstrating the complexity of the physics associated with segregation, in bidisperse mixtures of spherical particles that vary in both volume and density, the segregation direction depends not only on the volume ratio and density ratio, but also on the species concentration [60–63]. Therefore the physics of segregation is, at least in part, dependent on both the geometry, generated by the volume difference, and the mass (or density) difference between particle species, each driving segregation in different directions. But this complex interaction is not understood even for single intruder particles in spherical particle systems. It not only depends on relative sizes and densities, but also seems related to both particle contacts and flow kinematics [59]. The physics is potentially even more complicated for the more diverse particle contact interactions associated with nonspherical particles.

Returning to the validation examples in Fig. 4, validation case 2 (middle figure) corresponds to particles with  $R_V = 1$ , which implies that segregation should be minimal. Nevertheless, the deposited concentration for particle  $D1$  is somewhat below 50% in the upstream half of the heap (small  $x/L$ ) and gradually increases to slightly above 50% near the downstream end wall (large  $x/L$ ) in both simulation and experiment, which clearly indicates that some segregation is occurring. However, this is a result of the sidewalls. When the same particles are simulated with periodic sidewall boundary conditions, no segregation occurs, as expected from the volume ratio, and the deposited concentrations of both species are equal (and necessarily, invariant) along the entire length of the heap. This result demonstrates that sidewall boundaries affect segregation, consistent with previous results for spheres [19,64,65], and is discussed in more detail for nonspherical particles in the next section.

Further note that in validation case 2, the sidewalls promote segregation when  $R_V$  predicts no segregation, while the data for mixtures of equal diameter rods varying in length [11] suggests that the sidewalls reduce segregation relative to the prediction based on  $R_V$  (green diamonds in Fig. 12). The wall effect may be amplified in the case of rodlike particles because they tend to align their axes with the wall and disklike particles tend to align their circular faces against the wall. In both cases, these results demonstrate how bounding walls can affect the segregation.

## B. Continuum segregation model for nonspherical particles

Now that the segregation length scale  $S_i$  can be predicted for mixtures of nonspherical particles, the next question is if the advection-diffusion-segregation continuum model, Eq. (1), can be successfully applied. To answer this we consider the validation cases in Table II. The model uses kinematics (based on flow rate and  $d_{s,eq}$ ) of spherical particles in a quasi-2D bounded heap [13,14,66], flow depth measured from DEM simulation ( $4.5L_{\min}$  for cases 1 and 3 and  $4L_{\min}$  for case 2, where  $L_{\min}$  is the minimum length or diameter of the simulated particles), and the diffusion coefficient for volume-equivalent spherical particles ( $D = 0.055\dot{\gamma}\bar{d}_{eq}$ , where  $\bar{d}_{eq}$  is the mean, local volume-equivalent spherical particle diameter) [67]. It is important to note that the model may be somewhat less accurate when the volume ratio is near 1 and shape effects are more significant [9], or in cases when particle orientation is evolving, such as the flowing layer in rotating tumblers. However, once the distribution of particle orientation is established, the model should be applicable to a wide range of gravity-driven free-surface flows, just as it is for spherical particles [2].

Figure 13 compares the concentration of  $D1$  particles deposited on the heap averaged across the span from the DEM simulation results for each validation case (solid black curve) and that predicted from the continuum model using both the value for  $S_i$  measured from DEM results for that case (solid blue curve) and the value predicted by  $R_V$  via Eq. (10) (dashed blue curve). The results are remarkable. For validation case 1, both the measured and predicted values for  $S_i$  correctly capture the approximate magnitude of deposited concentration and the location of the interface ( $c_{D1} = 0.5$ ) between higher concentrations of each particle species deposited on the heap. Similarly, for validation case 3, the value for  $S_i$  predicted from Eq. (10) captures the correct concentration



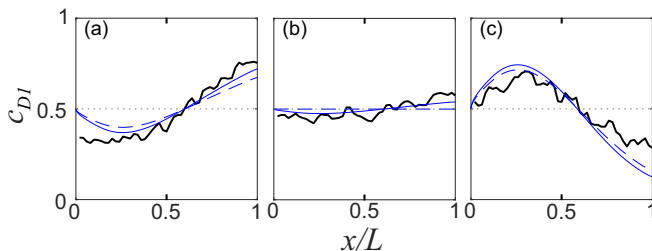


FIG. 13. Deposited concentration averaged across the span of disklike particles  $D1$  ( $d = 6.3$  mm,  $l = 3.2$  mm) for equal volume concentration bidisperse mixtures with three different rodlike particles from DEM simulation (black) and from Eq. (1) using the value for  $S_i$  measured directly from the simulation (solid blue) and the predicted  $S_i$  from Eq. (10) (dashed blue) for validation cases 1 (a), 2 (b), and 3 (c), see Table II.

magnitude and location of the interface between higher concentrations of each particle species. For validation case 2, where there should be no segregation ( $R_V = 1$ ), the measured value for  $S_i$  correctly captures the regions of higher species concentration for wall-bounded flow. However, as noted earlier, the predicted value for  $S_i$  based on  $R_V = 1$  predicts no segregation ( $c_{D1} = 0.5$ ) because wall effects are not taken into account. In fact, for all cases, the value of  $S_i$  predicted from Eq. (10) is slightly less than the value of  $S_i$  directly measured for the validation cases, so the deposited concentration is slightly reduced in magnitude. However, this is a consequence of the validation cases having planar sidewalls, while the value for  $S_i$  predicted from Eq. (10) is based on simulations with periodic boundary conditions to avoid sidewall effects. In spite of this, the results shown in Fig. 13 further validate the predictive capability of the continuum segregation model [Eq. (1)] and the segregation velocity model [Eqs. (2) and (10)], as well as demonstrate that the models can predict segregation of nonspherical particles when they are treated as volume-equivalent spherical particles.

### C. Reconciling with results for mixtures of sphere and cuboids

Finally, we discuss our findings in light of a recent study examining mixtures of cuboid and spherical particles in a rotating tumbler [8]. For cuboids with edge length equal to the sphere diameter, the authors report that the spheres segregate upward in the flowing layer and accumulate at the tumbler periphery [8]. This outcome is counter to the expectation for segregation based on the volume ratio  $R_V$ , as the volume of the cuboid is larger than the volume of the sphere. To better understand this result, we simulate an equal volume mixture of equal size cuboids ( $t = s = 8$ ,  $a = b = c = 1$  mm) and spheres ( $t = s = 2$ ,  $a = b = c = 1$  mm), corresponding to  $R_V = 1.8$  (accounting for the rounded edges of the superellipsoid cuboid in the volume) in bounded heap flow with both periodic and frictional sidewalls.

Figures 14(a) and 14(c), with frictional sidewalls, have a segregation pattern opposite to that expected based on  $R_V$ , matching the observation in the rotating tumbler [8]. That is, the concentration of spherical particles,  $c_s$ , deposited on the heap increases moving downstream. Close examination of the data in this case reveals that the deposited concentration of spherical particles varies across the span with highest concentration near the frictional sidewall. On the other hand, although the segregation is weak with periodic boundaries, shown in Figs. 14(b) and 14(d), the concentration of spheres deposited on the heap decreases slightly with downstream position, as expected for the smaller volume spherical particles. In this case, the measured segregation length scale is  $S_i/d_{s,eq} = 0.033$ , compared to the predicted value of  $S_i/d_{s,eq} = 0.048$  based on  $R_V = 1.8$  in Eq. (10). This difference, while significant, is not unreasonable when considered in light of the context of the range of particle shapes and values for  $S_i/d_{s,eq}$  in Fig. 12.

The impact of sidewalls is evident in the magnified image of the particles at the sidewall. The red cuboidal particles align with a face parallel to the frictional sidewall [Fig. 14(a)], which

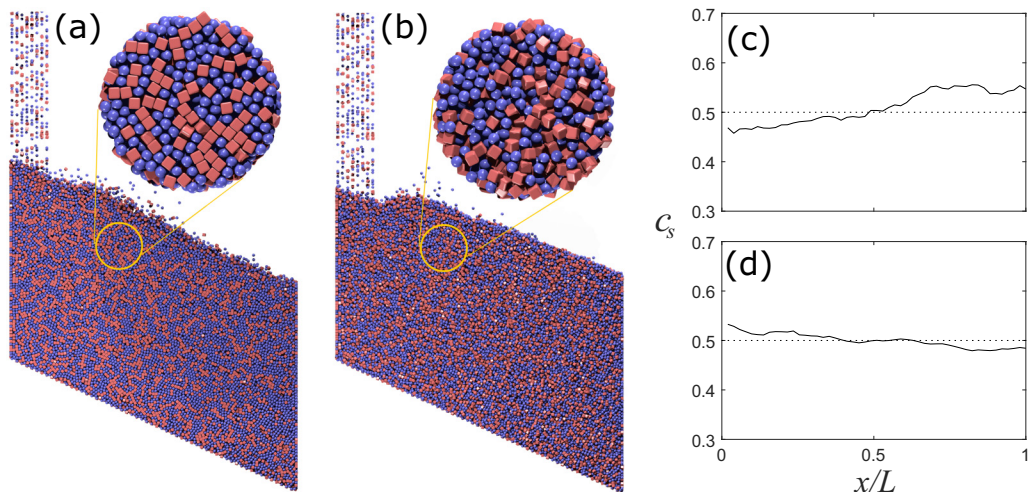


FIG. 14. DEM heap flow simulations of mixtures of spheres (blue) and cuboids (red) with (a) frictional sidewalls and (b) periodic sidewalls. Average concentration of deposited spheres  $c_s$  vs streamwise position  $x/L$  for (c) frictional sidewalls and (d) periodic sidewalls. Magnified particle images are shown for a portion of the flow along the sidewall (a) and along the periodic plane (b).

stands in sharp contrast to the random orientation evident with periodic sidewalls [Fig. 14(b)]. This boundary-driven alignment of the particle orientation at the sidewalls appears to explain the “reversed” segregation in Fig. 14(c) and in tumbler flow with sidewalls [8].

## VI. CONCLUSIONS

In this paper we present a detailed study of the degree of segregation over the multidimensional shape space for bidisperse mixtures of cylindrical particles, cylindrical and spherical particles, and spherical particles. We find that characterizing the propensity for segregation is much simpler than might be expected given the richness of the parameter space. First, the segregation velocity depends only on the shear rate and the concentration of the particle species [Eq. (2)], just as is the case for mixtures of spherical particles. Second, the segregation length scale  $S_i$  that characterizes the propensity for segregation depends only on the volume ratio of the two particles via the simple relation  $S_i/d_{s,eq} = C_* \ln(R_V)$ , Eq. (10), where  $C_* = 0.082$  is a universal constant across a wide range of cylindrical and spherical particle mixtures. The dependence of the segregation on the volume ratio of the particles aligns with a recent study that found that the primary driver of the lifting segregation force for a spherical intruder in a bed of spherical particles follows a buoyancylike scaling [59].

The similarity between the segregation rate for mixtures of particle species as different as cylinders (disklike and rodlike), spheres and cylinders, and spheres and spheres suggests that predicting segregation between differently shaped particles may be as simple as determining  $R_V$ , especially considering the diversity of the particle shapes and sizes shown in Fig. 1. It seems reasonable that generally spheroidal-like particles including those having faceted surfaces, ellipsoidal particles, tablet- or capsule-shaped particles, and seed- or grain-shaped particles would likely follow the same volume-ratio-based relation for the segregation velocity. After all, these particle shapes rarely differ from one another as much as the extreme examples of disks and rods differ from one another in Fig. 1, all of which follow the simple volume-ratio-based relation for  $S_i$ . Further study is needed to confirm this prediction, but if broadly applicable, such a relationship between  $R_V$  and  $S_i$  [i.e.,  $S_i/d_{s,eq} = C_* \ln(R_V)$ ] would be of great benefit to continuum modeling of segregation. However, this relationship may change drastically for extreme particle shapes, such as concave shapes, which can

interact through very different mechanisms, including cohesive interlocking behavior, for extremely large aspect ratio rods (fibers) that strongly align with the flow, or for other particle shapes that have the potential to locally jam.

Further study will be necessary to determine the range of volume ratios (near  $R_V = 1$ ) over which shape effects, such as those observed in the segregation of equal volume ellipsoids and spheroids [7] and of equal volume spheres with cubes, cuboids, and ellipsoids [9], are significant. Also of interest is determining if the segregation rates for bidisperse mixtures of cylindrical particles can be applied to multidisperse and polydisperse mixtures, similar to how the segregation rate between bidisperse mixtures of spherical particles can be applied to mixtures with more than two constituent species [18,24–26]. And finally, the influence of lateral bounding walls which, as shown here, can reverse the segregation direction compared to laterally unbounded flows for small  $R_V$ , needs to be better understood and characterized.

The results presented in this paper, particularly Fig. 12 and Eq. (10), demonstrate that the segregation of an important subset of all nonspherical particle mixtures, namely, cylinder mixtures and sphere-cylinder as well as sphere-sphere mixtures, can be simply predicted based on the relative volumes of the particles regardless of particle shape.

#### ACKNOWLEDGMENT

The authors gratefully acknowledge funding from the Dow Chemical Company and helpful discussions with Yi Fan and Karl Jacob.

- 
- [1] J. M. N. T. Gray, Particle segregation in dense granular flows, *Annu. Rev. Fluid Mech* **50**, 407 (2018).
  - [2] P. B. Umbanhowar, R. M. Lueptow, and J. M. Ottino, Modeling segregation in granular flows, *Annu. Rev. Chem. Biomol. Eng.* **10**, 129 (2019).
  - [3] G. M. Friedman, Distinction between dune, beach, and river sands from their textural characteristics, *J. Sediment. Res.* **31**, 514 (1961).
  - [4] P. Tang and V. M. Puri, Methods for minimizing segregation: A review, *Part. Sci. Technol.* **22**, 321 (2004).
  - [5] J. J. McCarthy, Turning the corner in segregation, *Powder Technol.* **192**, 137 (2009).
  - [6] H.-G. Matuttis, N. Ito, and H. Watanabe, Shape segregation for bidisperse mixtures of ellipses in two dimensions, *Proceedings of Traffic and Granular Flow '01*, edited by M. Fukui, Y. Sugiyama, M. Schreckenberg, and D. E. Wolf (Springer-Verlag Berlin Heidelberg, 2003), pp. 455–460.
  - [7] S. Y. He, J. Q. Gan, D. Pinson, and Z. Y. Zhou, Particle shape-induced radial segregation of binary mixtures in a rotating drum, *Powder Technol.* **341**, 157 (2019).
  - [8] G. G. Pereira and P. W. Cleary, Segregation due to particle shape of a granular mixture in a slowly rotating tumbler, *Granular Matter* **19**, 23 (2017).
  - [9] G. Lu and C. R. Müller, Particle-shape induced radial segregation in rotating cylinders, *Granular Matter* **22**, 50 (2020).
  - [10] M. Alizadeh, A. Hassanpour, M. Pasha, M. Ghadiri, and A. Bayly, The effect of particle shape on predicted segregation in binary powder mixtures, *Powder Technol.* **319**, 313 (2017).
  - [11] Y. Zhao, H. Xiao, P. B. Umbanhowar, and R. M. Lueptow, Simulation and modeling of segregating rods in quasi-2D bounded heap flow, *AIChE J.* **64**, 1550 (2018).
  - [12] C. P. Schlick, Y. Fan, P. B. Umbanhowar, J. M. Ottino, and R. M. Lueptow, Granular segregation in circular tumblers: Theoretical model and scaling laws, *J. Fluid Mech.* **765**, 632 (2015).
  - [13] Y. Fan, C. P. Schlick, P. B. Umbanhowar, J. M. Ottino, and R. M. Lueptow, Modelling size segregation of granular materials: The roles of segregation, advection and diffusion, *J. Fluid Mech.* **741**, 252 (2014).
  - [14] C. P. Schlick, Y. Fan, A. B. Isner, P. B. Umbanhowar, J. M. Ottino, and R. M. Lueptow, Modeling segregation of bidisperse granular materials using physical control parameters in the quasi-2D bounded heap, *AIChE J.* **61**, 1524 (2015).

- [15] H. Xiao, P. B. Umbanhowar, J. M. Ottino, and R. M. Lueptow, Modelling density segregation in flowing bidisperse granular materials, *Proc. R. Soc. A* **472**, 20150856 (2016).
- [16] S. B. Savage and C. K. K. Lun, Particle size segregation in inclined chute flow of dry cohesionless granular solids, *J. Fluid Mech.* **189**, 311 (1988).
- [17] Y. Liu, M. Gonzalez, and C. Wassgren, Modeling granular material segregation using a combined finite element method and advection-diffusion-segregation equation model, *Powder Technol.* **346**, 38 (2019).
- [18] Z. Deng, P. B. Umbanhowar, J. M. Ottino, and R. M. Lueptow, Continuum modelling of segregating tridisperse granular chute flow, *Proc. R. Soc. A* **474**, 20170384 (2018).
- [19] A. B. Isner, P. B. Umbanhowar, J. M. Ottino, and R. M. Lueptow, Granular flow in a wedge-shaped heap: Velocity field, kinematic scalings, and segregation, *AIChE J.* **66**, e16912 (2020).
- [20] A. M. Fry, P. B. Umbanhowar, J. M. Ottino, and R. M. Lueptow, Effect of pressure on segregation in granular shear flows, *Phys. Rev. E* **97**, 062906 (2018).
- [21] A. M. Fry, P. B. Umbanhowar, J. M. Ottino, and R. M. Lueptow, Diffusion, mixing, and segregation in confined granular flows, *AIChE J.* **65**, 875 (2019).
- [22] H. Xiao, Y. Fan, K. V. Jacob, P. B. Umbanhowar, M. Kodam, J. F. Koch, and R. M. Lueptow, Continuum modeling of granular segregation during hopper discharge, *Chem. Eng. Sci.* **193**, 188 (2019).
- [23] Z. Deng, Y. Fan, J. Theuerkauf, K. V. Jacob, P. B. Umbanhowar, and R. M. Lueptow, Modeling segregation of polydisperse granular materials in hopper discharge, *Powder Technol.* **374**, 389 (2020).
- [24] Z. Deng, P. B. Umbanhowar, J. M. Ottino, and R. M. Lueptow, Modeling segregation of polydisperse granular materials in developing and transient free-surface flows, *AIChE J.* **65**, 882 (2019).
- [25] C. P. Schlick, A. B. Isner, B. J. Freireich, Y. Fan, P. B. Umbanhowar, J. M. Ottino, and R. M. Lueptow, A continuum approach for predicting segregation in flowing polydisperse granular materials, *J. Fluid Mech.* **797**, 95 (2016).
- [26] S. Gao, J. M. Ottino, P. B. Umbanhowar, and R. M. Lueptow, Modeling granular segregation for overlapping species distributions, *Chem. Eng. Sci.* **231**, 116259 (2021).
- [27] P. Gajjar and J. M. N. T. Gray, Asymmetric flux models for particle-size segregation in granular avalanches, *J. Fluid Mech.* **757**, 297 (2014).
- [28] R. P. Jones, A. B. Isner, H. Xiao, J. M. Ottino, P. B. Umbanhowar, and R. M. Lueptow, Asymmetric concentration dependence of segregation fluxes in granular flows, *Phys. Rev. Fluids* **3**, 094304 (2018).
- [29] R. P. Jones, J. M. Ottino, P. B. Umbanhowar, and R. M. Lueptow, Remarkable simplicity in the prediction of non-spherical particle segregation, *Phys. Rev. Res.* **2**, 042021(R) (2020).
- [30] J. Rodriguez, T. Edeskär, and S. Knutsson, Particle shape quantities and measurement techniques: A review, *Electron. J. Geotech. Eng.* **18/A**, 169 (2013).
- [31] F. N. Altuhafi, M. R. Coop, and V. N. Georgiannou, Effect of particle shape on the mechanical behavior of natural sands, *J. Geotech. Geoenviron. Eng.* **142**, 04016071 (2016).
- [32] P. A. Cundall and O. D. L. Strack, Discrete numerical model for granular assemblies, *Géotechnique* **29**, 47 (1979).
- [33] Y. Guo and J. S. Curtis, Discrete element method simulations for complex granular flows, *Annu. Rev. Fluid Mech.* **47**, 21 (2015).
- [34] J. Schafer, S. Dippel, and D. E. Wolf, Force schemes in simulations of granular materials, *J. Phys. I*, 5 (1996).
- [35] L. E. Silbert, G. S. Grest, R. Brewster, and A. J. Levine, Rheology and Contact Lifetimes in Dense Granular Flows, *Phys. Rev. Lett.* **99**, 068002 (2007).
- [36] G. H. Ristow, in *Pattern Formation in Granular Materials*, Springer Tracts in Modern Physics Vol. 164 (Springer-Verlag, Berlin Heidelberg, 2000).
- [37] G. Lu, J. R. Third, and C. R. Müller, Discrete element models for non-spherical particle systems: From theoretical developments to applications, *Chem. Eng. Sci.* **127**, 425 (2015).
- [38] Y. Zhao, L. Xu, P. B. Umbanhowar, and R. M. Lueptow, Discrete element simulation of cylindrical particles using super-ellipsoids, *Particuology* **46**, 55 (2019).
- [39] M. Kodam, R. Bharadwaj, J. Curtis, B. Hancock, and C. Wassgren, Force model consideration for glued-sphere discrete element method simulations, *Chem. Eng. Sci.* **64**, 3466 (2009).

- [40] M. Kodam, R. Bharadwaj, J. Curtis, B. Hancock, and C. Wassgren, Cylindrical object contact detection for use in discrete element method simulations, Part I: Contact detection algorithms, *Chem. Eng. Sci.* **65**, 5852 (2010).
- [41] M. Kodam, R. Bharadwaj, J. Curtis, B. Hancock, and C. Wassgren, Cylindrical object contact detection for use in discrete element method simulations, Part II: Experimental validation, *Chem. Eng. Sci.* **65**, 5863 (2010).
- [42] Y. You and Y. Zhao, Discrete element modelling of ellipsoidal particles using super-ellipsoids and multi-spheres: A comparative study, *Powder Technol.* **331**, 179 (2018).
- [43] G. Lu, J. R. Third, and C. R. Müller, Critical assessment of two approaches for evaluating contacts between super-quadric shaped particles in DEM simulations, *Chem. Eng. Sci.* **78**, 226 (2012).
- [44] P. W. Cleary, Particulate mixing in a plough share mixer using DEM with realistic shaped particles, *Powder Technol.* **248**, 103 (2013).
- [45] A. Podlozhnyuk, S. Pirker, and C. Kloss, Efficient implementation of superquadric particles in discrete element method within an open-source framework, *Comput. Part. Mech.* **4**, 101 (2017).
- [46] S. Wang, Y. Fan, and S. Ji, Interaction between super-quadric particles and triangular elements and its application to hopper discharge, *Powder Technol.* **339**, 534 (2018).
- [47] H. Chen, S. Zhao, and X. Zhou, DEM investigation of angle of repose for super-ellipsoidal particles, *Particuology* **50**, 53 (2020).
- [48] P. W. Cleary, Large scale industrial DEM modelling, *Eng. Comput.* **21**, 169 (2004).
- [49] A. H. Barr, Superquadrics and angle-preserving transformations, *IEEE Comput. Graph. Appl.* **1**, 11 (1981).
- [50] A. Jaklič and F. Solina, Moments of superellipsoids and their application to range image registration, *IEEE Trans. Syst. Man Cybern. Part B Cybern.* **33**, 648 (2003).
- [51] S. Zhao, N. Zhang, X. Zhou, and L. Zhang, Particle shape effects on fabric of granular random packing, *Powder Technol.* **310**, 175 (2017).
- [52] G. T. Houlsby, Potential particles: A method for modelling non-circular particles in DEM, *Comput. Geotech.* **36**, 953 (2009).
- [53] X. Lin and T.-T. Ng, Contact detection algorithms for three-dimensional ellipsoids in discrete element modelling, *Int. J. Num. Anal. Meth. Geomech.* **19**, 653 (1995).
- [54] G. A. Kohring, S. Melin, H. Puhl, H. J. Tillemans, and W. Vermöhlen, Computer simulations of critical, non-stationary granular flow through a hopper, *Comput. Methods Appl. Mech. Eng.* **124**, 273 (1995).
- [55] R. L. Norton, *Machine Design an Integrated Approach*, 2nd ed. (Pearson Education, Singapore, 2003).
- [56] Y. Fan, Y. Boukerkour, T. Blanc, P. B. Umbanhowar, J. M. Ottino, and R. M. Lueptow, Stratification, segregation, and mixing of granular materials in quasi-two-dimensional bounded heaps, *Phys. Rev. E* **86**, 051305 (2012).
- [57] POV-Ray—The Persistence of Vision Raytracer, <http://www.povray.org>, v3.7.
- [58] T. Weinhart, A. R. Thornton, S. Luding, and O. Bokhove, From discrete particles to continuum fields near a boundary, *Granul. Matter* **14**, 289 (2012).
- [59] L. Jing, J. M. Ottino, R. M. Lueptow, and P. B. Umbanhowar, Rising and sinking intruders in dense granular flows, *Phys. Rev. Res.* **2**, 022069 (2020).
- [60] N. Thomas, Reverse and intermediate segregation of large beads in dry granular media, *Phys. Rev. E* **62**, 961 (2000).
- [61] A. Tripathi and D. V. Khakhar, Density difference-driven segregation in a dense granular flow, *J. Fluid Mech.* **717**, 643 (2013).
- [62] D. R. Tunuguntla and A. R. Thornton, Balancing size and density segregation in bidisperse dense granular flows, *EPJ Web Conf.* **140**, 03079 (2017).
- [63] Y. Duan, P. B. Umbanhowar, J. M. Ottino, and R. M. Lueptow, Modelling segregation of flowing bidisperse granular mixtures varying simultaneously in size and density, *J. Fluid Mech.* **918**, A20 (2021).
- [64] A. M. Fry, V. Vidyapati, J. P. Hecht, P. B. Umbanhowar, J. M. Ottino, and R. M. Lueptow, Measuring segregation characteristics of industrially relevant granular mixtures: Part I. A continuum model approach, *Powder Technol.* **368**, 190 (2020).

- [65] A. B. Isner, P. B. Umbanhowar, J. M. Ottino, and R. M. Lueptow, Axisymmetric granular flow on a bounded conical heap: Kinematics and size segregation, [Chem. Eng. Sci. \*\*217\*\*, 115505 \(2020\)](#).
- [66] Y. Fan, P. B. Umbanhowar, J. M. Ottino, and R. M. Lueptow, Kinematics of monodisperse and bidisperse granular flows in quasi-two-dimensional bounded heaps, [Proc. R. Soc. A \*\*469\*\*, 20130235 \(2013\)](#).
- [67] Y. Fan, P. B. Umbanhowar, J. M. Ottino, and R. M. Lueptow, Shear-Rate-Independent Diffusion in Granular Flows, [Phys. Rev. Lett. \*\*115\*\*, 088001 \(2015\)](#).